arXiv:2607.18594v1 [cond-mat.mtrl-sci] 21 Jul 2026

Data-driven Design of Metal-Organic Frameworks with Tunable Negative Thermal Expansion

Prathami Divakar Kamath[1,2], Francesco Tavani[3,4,5], Alin Marin Elena[6], Théo Jaffrelot Inizan[2,3,4], Yen-hsu Lin[3], Jian Yin[3], Wenqian Xu[7], Omar M. Yaghi[3,†], Kristin A. Persson[1,2,†]

[1]Department of Materials Science & Engineering, University of California, Berkeley, CA, USA
[2]Materials Sciences Division, Lawrence Berkeley National Laboratory, Berkeley, CA, USA
[3]Department of Chemistry, University of California, Berkeley, CA, USA
[4]Bakar Institute of Digital Materials for the Planet, Division of Computing, Data Science, and Society, University of California, Berkeley, CA, USA
[5]Dipartimento di Chimica, Università degli Studi di Roma La Sapienza, P.le A. Moro 5, I-00185, Rome, Italy
[6]Scientific Computing Department, Science and Technology Facilities Council, Daresbury Laboratory, UK
[7]X-ray Science Division, Advanced Photon Source, Argonne National Laboratory, Lemont, IL, USA

[†] Corresponding author: yaghi@berkeley.edu, kapersson@lbl.gov

Abstract

Materials with negative thermal expansion (NTE) are essential for applications requiring precise control of thermal expansion. Owing to their exceptional chemical tunability, flexible architectures, and low-energy lattice vibrations, metal–organic frameworks (MOFs) represent a rich platform for exploring NTE. However, uncovering the structural motifs that govern NTE across the enormous MOF design space remains experimentally challenging, and large-scale first-principles phonon calculations are computationally prohibitive. Here, we comprehensively evaluate the factors influencing NTE in MOFs by utilizing a high-throughput workflow based on MACE-MP-MOF0, a machine learning interatomic potential fine-tuned for MOFs with near-ab initio accuracy, to construct PhononMOFdb, a database of phonons, inelastic neutron scattering spectra, bulk moduli, and heat capacities for over 12,000 MOFs. High-throughput screening of this database reveals that highly porous cubic topology frameworks with heavier, lower-valent metal nodes favor strong NTE, while linker functionalization provides a practical handle for tuning NTE magnitude and sign without compromising mechanical stability. Experimental validation via high-resolution temperature-dependent synchrotron powder X-ray diffraction on the Ce-UiO-66 MOF and its brominated variants confirms the design recipe and yields volumetric NTE coefficients surpassing current records. This work establishes a data-driven strategy for engineering NTE in MOFs, showing how machine learning-accelerated discovery and targeted experimental validation together unlock predictive materials design.

1. Introduction

Negative Thermal Expansion (NTE)[1–3] materials contract upon heating and are of significant interest because they enable precise control of thermal expansion in composites for applications including precision optics, microelectronics, and aerospace engineering.[4–8] While NTE is uncommon in conventional solids, it is widely observed in metal-organic frameworks (MOFs),[9–11] which are ultra-porous materials with exceptional structural tunability and flexibility.[12–14] The flexible nature of the MOF struc-

tures gives rise to a high density of low-frequency phonons,[15,16] which are collective atomic vibrations that govern how a crystal responds to heat,[17,18] making MOFs ideal candidates for tuning NTE. Enhancing NTE is desirable for designing zero thermal expansion composites,[19] whereas suppressing NTE can mitigate excessive thermal contraction and improve MOF stability.[20] Despite the widespread occurrence of NTE in MOFs, achieving systematic and predictive control over its magnitude and sign remains challenging due to the large chemical space for exploration and expensive phonon computations.[21,22]

Although experimental strategies based on local node distortion,[23,24] mixed-linker solid solutions,[25] defect engineering,[26] and framework retrofitting[27] have successfully tuned NTE in MOFs, these approaches have primarily been demonstrated within specific material families and are not yet readily generalizable across the broader MOF chemical space. Furthermore, NTE measurements for a given MOF may vary with sample crystallinity, defect density, and thermal history,[28] making it difficult to benchmark quantitative models. High-throughput computational screening[29] and targeted mechanistic studies[10,20,24] have established that NTE arises predominantly from low-energy transverse linker phonons and rigid-unit modes (RUMs),[22,30] yet these theoretical investigations relied on classical force fields[31,32] known to be affected by larger errors in the modeling of MOF phonons compared to density functional theory (DFT).[33,34] Further, existing DFT phonon datasets[35,36] cover only a small fraction of the MOF chemical space, and the approximations required for large-scale calculations frequently introduce spurious imaginary modes that corrupt derived thermal properties.[37] Machine learning interatomic potentials[38,39] now bridge the computational gap, with MACE-MP-MOF0[21] delivering ab initio-quality phonons and derived thermal and mechanical properties at a fraction of the DFT cost. Nevertheless, a transferable, phonon-centric design methodology for predictively tuning NTE across a broad MOF chemical space remains absent.

In this work, we leverage MACE-MP-MOF0 (a fine-tuned MACE-MP-0[40] model on MOF structures for accurate phonon predictions) to construct PhononMOFdb, the largest MOF phonon database to date, comprising ∼12,000 structures with phonon densities of states (DOS), band structures, heat capacities, and derived vibrational thermodynamic quantities, along with bulk moduli and inelastic neutron scattering (INS) spectra validated against DFT and experiments. This database enables a vibration-based screening strategy that identifies the low-frequency modes governing NTE and reveals that heavy metal nodes in cubic, high-porosity topologies amplify their contributions. We show that systematic linker functionalization continuously tunes thermal expansion, including negative to positive transitions, without altering original framework stability. We validate these design principles with high-resolution synchrotron powder X-ray diffraction (PXRD) experiments on Ce-UiO-66 and two of its brominated variants that confirm our predictions of decreased NTE with increased bromine loading due to suppressed RUMs and transverse vibrations. Large anharmonic displacements at higher temperatures in Ce-UiO-66-Br yield an exceptional volumetric NTE coefficient of -593(25) $(MK)^{-1}$, surpassing previously reported MOF NTE records. Altogether, this work establishes a data-driven, phonon-centric framework for tuning thermal expansion across diverse MOFs, demonstrating how computational predictions can guide experimental realization of targeted NTE behavior.

2. Materials and Methods

2.1. PhononMOFdb Generation

PhononMOFdb was generated by applying the MACE-MP-MOF0 (v2) model[21] to ∼12,000 computation-ready MOFs from the QMOF database,[41,42] spanning the model's valid chemical space. Harmonic phonon spectra and derived thermal properties were computed using Phonopy.[43,44] More than 78% of the structures are dynamically stable, with only ∼11% exhibiting an imaginary-mode fraction exceeding 0.1%. In addition, bulk moduli were obtained via the Birch–Murnaghan equation of state using seven volumes spanning ±3% linear strain about the equilibrium volume. INS spectra were simulated at 10 K using ABINS within MANTID,[45,46] employing a TOSCA-geometry incoherent approximation including two-phonon transitions.[47] Additional details are provided in Section 1 of the SI.

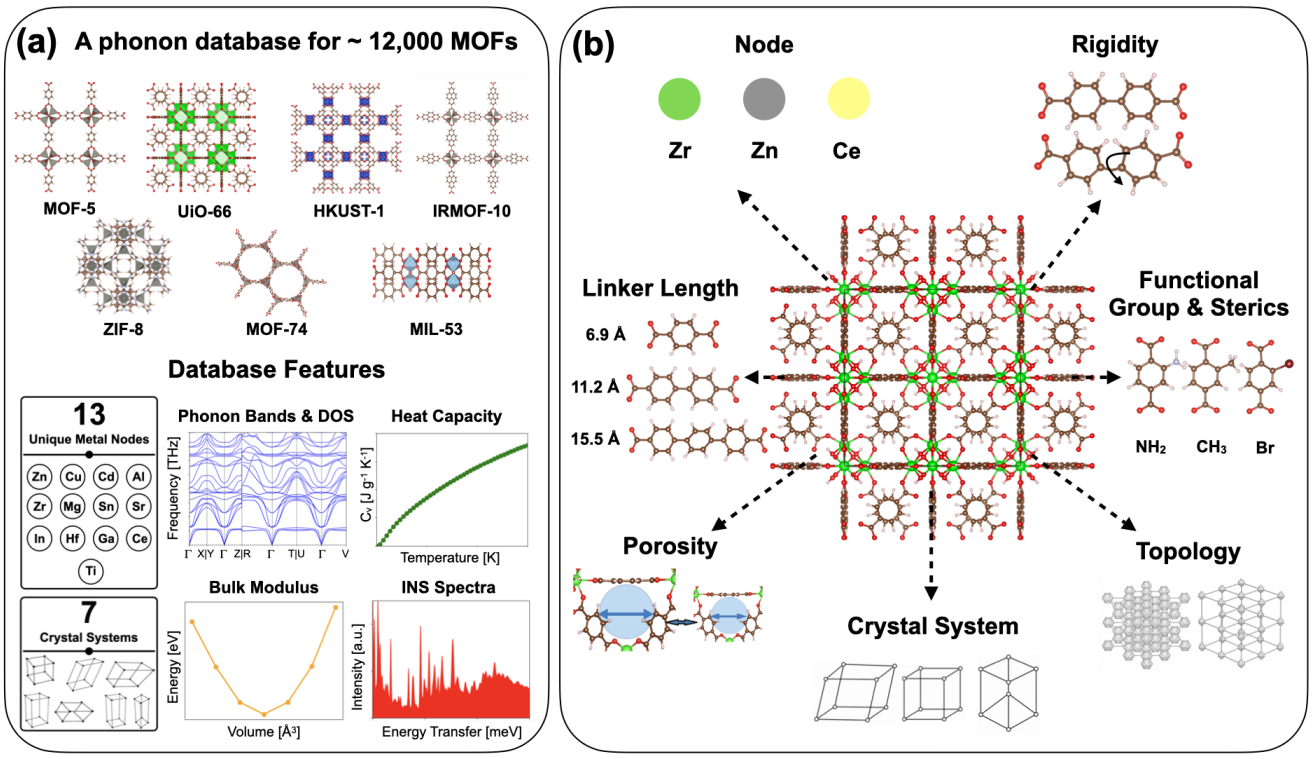

Figure 1: (a) Overview of the PhononMOFdb database, consisting of phonons and thermophysical properties for over 12,000 MOFs. All seven crystal systems are covered with the following distribution: 46.9% triclinic, 37.5% monoclinic, 8.2% orthorhombic, 2.8% trigonal, 2.7% tetragonal, 1.3% hexagonal and 0.6% cubic (b) Schematic representation of the data-driven screening workflow: seven tunable structural descriptors are systematically analyzed against the low-frequency vibrational landscape to identify colossal NTE candidates.

2.2. DFT phonon computations

The DFT INS data to benchmark PhononMOFdb accuracy was generated for ZIF-8 from harmonic phonons computed with the VASP 6.4.2 package.[48–51] The PBE density functional[52] with D3(BJ)[53,54] empirical dispersion correction was applied to account for long-range van der Waals interactions. The energy convergence was set to 10^{-8} eV for the self-consistent field (SCF) cycles, and the force convergence was set to -0.02 eV/Å for a tight structural relaxation. A $2\times2\times2$ supercell containing 1104 atoms was used on the primitive cell for finite difference phonon calculations with Phonopy.

2.3. MOF synthesis and synchrotron PXRD characterization

The Ce-UiO-66-X (X = H, Br, 2Br) MOFs were synthesized following a previously reported solvothermal procedure, using dimethylformamide as solvent.[55] The MOF phase purity and crystallinity were verified by laboratory-based PXRD measurements. Synchrotron PXRD measurements were performed using a wavelength of 0.2099 Å on beamline 11-ID-B at the Advanced Photon Source (APS), Argonne National Laboratory. Calibration of the PXRD patterns was performed with CeO_2 powder as a standard, and GSAS-II[56] was employed for azimuthal integration. The samples were loaded into 1.0 mm Kapton tubes prior to data collection. Temperature-dependent PXRD data were collected from 100 to 350 K at 50 K intervals. Lattice parameters were extracted at each temperature via Le Bail refinement using GSAS-II (Figure S1), with residuals $w_R \leq 4.5\%$ across all fits (Table S1-3). Volumetric thermal expansion coefficients α_V were computed from the refined lattice parameters using a finite difference approach.

3. Results and Discussion

3.1. Database Generation and High-Throughput Screening

As illustrated in Figure 1a, PhononMOFdb covers all seven crystal systems, moving beyond previous

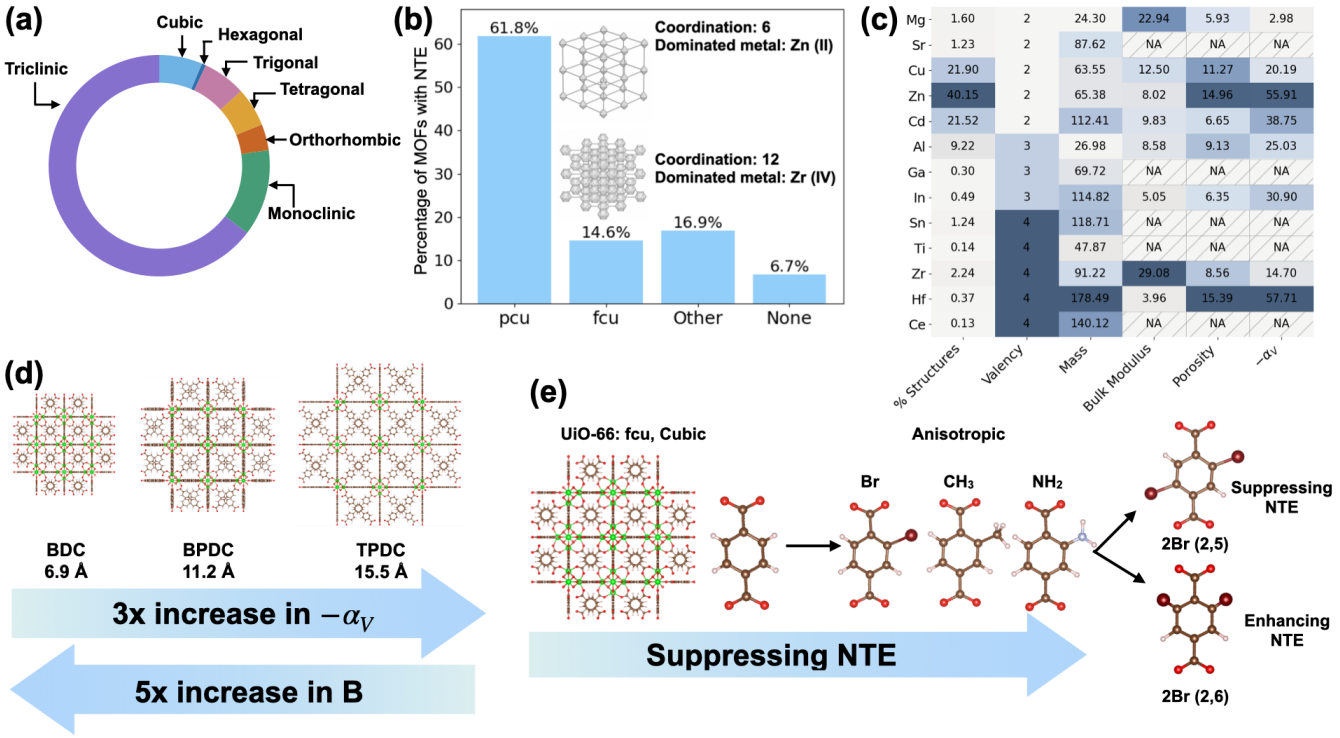

Figure 2: (a) Distribution of volumetric NTE candidates across all seven crystal systems (43.9% triclinic, 40.7% monoclinic, 8.6% orthorhombic, 2.8% trigonal, 2.5% tetragonal, 1.0% hexagonal, 0.5% cubic). (b) Distribution of NTE candidates by topology where "None" denotes structures with unassigned topologies. (c) Metal-node descriptor matrix where colors are normalized independently for each column, with darker shades indicating larger values. (d) Effect of isoreticular linker elongation on NTE and bulk modulus. (e) Linker functionalization enables systematic tuning of NTE magnitude and sign. The corresponding NTE values for each structure in (d) and (e) are listed in Tables S7–S8.

work mainly focused on isoreticular cubic MOFs.[10] The database includes thirteen unique metal nodes with diverse linkers and functional groups which enables an extensive study of how structural factors influence the vibrational landscape of MOFs. The heat capacities of MOFs in PhononMOFdb can be used to estimate the energy penalty associated with adsorbent retrieval[35,37] while the bulk moduli provide an estimate for the MOF mechanical stability.[57] The reliability of MACE-MP-MOF0 for predicting the aforementioned properties relative to experiments has been demonstrated in previous studies.[21,37,39] Here, we validate the accuracy of INS spectra in PhononMOFdb by benchmarking against both DFT and experimental measurements.

In MOFs, inelastic neutron scattering (INS) has been widely used to characterize framework lattice dynamics, gas adsorption, and adsorbate-induced changes in vibrational spectra.[58–61] MOF-5 and ZIF-8 are among the most extensively studied MOFs by INS[62–67] and are therefore used here as benchmark systems. Both MACE-MP-MOF0 and DFT accurately reproduce the overall spectral features for MOF-5 and ZIF-8, with a modest red shift of ≤ 1.8 meV relative to experiments which is a well-known consequence of the PBE functional[68,69] (Figure S2 and Table S4). Since broadly accessible experimental INS data for MOFs remain limited,[70] PhononMOFdb provides an open-access resource for INS spectra with a released workflow to enable extension to additional MOFs beyond the current dataset.

While isotropic MOFs are capable of exhibiting large NTE,[10] the vast diversity of MOFs also includes anisotropic frameworks that can exhibit linear or areal NTE while maintaining an overall non-negative volumetric expansion coefficient.[71] Although less explored, the mechanism for observing NTE in anisotropic MOFs has been attributed to a combination of low-frequency transverse linker vibrations and RUMs,[72] predominantly in the 0–2 THz range.[22] This is consistent with the previously identified mechanisms in isoreticular MOFs[10,11] sug-

gesting a common phonon-driven origin of NTE across diverse MOF families.

Motivated by these observations, we leverage the low-frequency (0–2 THz) harmonic phonon data in PhononMOFdb to develop a computationally efficient screening strategy for volumetric NTE. We first validate this approach by computing phonon DOS for MOF-5, UiO-66, and MOF-74 for which experimental thermal expansion data are available (Figure S3a). MOF-5 and UiO-66 exhibit volumetric NTE[24,73] and display pronounced DOS features in the 0–2 THz range, whereas MOF-74, which exhibits near-zero thermal expansion,[22,74] shows negligible DOS in the same range. We build on this correlation and screen a representative subset of 7000 MOFs from PhononMOFdb (see Table S5) for intense low-frequency phonon modes and apply the quasi-harmonic approximation (QHA) for NTE calculations only to MOF structures passing this initial filter. As shown in Figure S3b, the QHA calculations reproduce the experimental trends of NTE across several well-characterized MOFs. In order to address the challenge of achieving large NTE without softening the framework to the point of mechanical failure,[20,75] we apply a bulk modulus threshold of $B \geq 1$ GPa at 100 K to the 390 screened MOFs reducing the pool to 178 mechanically stable volumetric NTE candidates.

To investigate the molecular-level origins of NTE, we then sequentially analyze the dependence of the NTE coefficient α_V on seven structural descriptors for the diverse screened frameworks, including MOF crystal system, topology, metal node identity, linker length, flexibility and functionalization (see Figure 1b).

3.1.1 Step 1: Role of Crystal System

Figure 2a shows the crystal system distribution of the 178 screened MOFs with volumetric NTE. Colossal NTE is not confined to cubic frameworks, which dominate the experimental literature,[72] but extends across all seven crystal systems with a majority of the triclinic and monoclinic MOFs exhibiting the largest NTE magnitudes (Figure S4a). As shown in Figure S4b, this trend may be primarily attributed to the highly anisotropic nature of the QMOF database, which provides a largely unexplored chemical space for volumetric NTE in non-cubic MOFs. We find eleven MOFs as candidates for colossal volumetric NTE (defined here as $|\alpha_V| \geq 100$), highlighting the untapped potential of anisotropic MOFs for extreme volumetric NTE. The eleven colossal NTE candidates span triclinic, monoclinic, trigonal, tetragonal, and cubic crystal systems, suggesting that crystal system alone is insufficient to explain large NTE and motivating a search for common governing structural features.

3.1.2 Step 2: Topology and Metal Node Effects

We next analyze MOF topology, which encodes node–linker connectivity and is less sensitive than crystal systems to geometric distortions. As shown in Fig. 2b, topology serves as a more robust descriptor for NTE trends, with 61.8% of screened MOFs adopting the primitive cubic (**pcu**) topology, followed by face-centered cubic (**fcu**). Notably, seven of the eleven colossal NTE MOFs are also **pcu** frameworks despite differing crystal systems, highlighting a clear structure–property correlation.

The screened **pcu** frameworks are almost exclusively Zn-based, consistent with the preference of Zn^{2+} for sixfold coordination, whereas all **fcu** MOFs contain Zr^{4+} nodes that form stable 12-coordinate clusters. On average, we find that the large majority of **pcu** MOFs follows from large uniform pores and soft frameworks enabled by this topology (see Table S6) which favor large transverse vibrations and enhance NTE. The **fcu** MOFs exhibit higher bulk moduli and lower volumetric NTE than **pcu** frameworks, consistent with the weaker Zn^{2+} coordination environment relative to the high-valent Zr^{4+} nodes, whose larger charge density produces stronger metal–ligand bonding[76] and stiffens the framework. This trend is corroborated by the two best-characterized volumetric NTE MOFs in the experimental literature, namely MOF-5 (**Zn-pcu**)[62] and UiO-66 (**Zr-fcu**),[24] which exhibit large and moderate NTE, respectively. The **fcu** topology therefore represents a viable design target when mechanical stability is a priority.

Figure 2c displays the metal node distribution of the MOFs selected from the screening. Given that the QMOF database exhibits an uneven distribution of metal node identity, five metals (i.e., Sr, Ga, Sn, Ti and Ce) yield no screened candidates and are labeled "NA", reflecting the limited screening pool rather than intrinsically unfavorable NTE. The remaining 178 candidates span eight distinct metal nodes. The largest average NTE magnitudes are

found in Zn- and Hf-based MOFs, consistent with their larger average pore volumes in the descriptor matrix of Figure 2c and the established correlation between porosity and NTE.[20]

Beyond porosity, the metal node identity influences the dynamics of the MOF lattice through the harmonic frequency relationship $(\omega) \propto \sqrt{k/m}$, where k is the stiffness of the effective bond and m the atomic mass. Consequently, metal nodes with lower charge such as Zn and Cu exhibit lower bulk moduli and larger NTE if compared to tetravalent nodes with higher charge such as Zr when atomic masses are similar. As illustrated in Figure 2c, in MOFs based on substantially heavier nodes such as Hf the larger atomic mass of the metal sites compensates for their higher charge, overall lowering the vibrational frequencies and enhancing NTE. Consequently, for a given topology, coordination geometry and valency, choosing a heavier metal node provides a further handle for enhancing NTE. This trend further suggests that heavier tetravalent analogues within the fcu family, such as Ce and Hf, should exhibit larger NTE than their lighter Zr and Ti counterparts by extrapolation.

3.1.3 Step 3: Linker Effects

We next explore linker chemistry as an additional tunable handle to enhance NTE for a given MOF topology and metal node. Longer linkers and increased porosity have been shown to generally favor larger NTE in previous studies.[20,25] As illustrated in Figure 2d, systematic isoreticular expansion of the linkers from 1,4-benzenedicarboxylate (BDC) in UiO-66 to 1,4-Di(4-carboxyphenyl)benzene (TPDC) in UiO-68 leads to an approximately three-fold increase in NTE but simultaneously reduces the bulk modulus by nearly a factor of five. Based on these findings, organic linker elongation is a viable route for enhancing NTE in MOFs with exceptionally high stiffness such as UiO-66 (∼35 GPa). However, this strategy is unlikely to be transferable to MOFs with intrinsically lower bulk moduli, where further mechanical softening would compromise structural integrity (see Figure S5 and Table S7).

We then analyze linker functionalization as a tool to modify the underlying lattice dynamics and NTE behavior without compromising the mechanical stability of the core framework. The screened **pcu** and **fcu** MOFs (see Figure S6) predominantly feature BDC-derived linkers incorporating bulky side groups, extended conjugated backbones, as well as electron-donating (-OH, -NH_2 and -CH_3) and electron-withdrawing substituents (-F, -Cl, -Br).

To better understand how MOF linker functionalization influences NTE, we substitute the H atom in the para-position of the BDC linker in the **fcu** UiO-66 with X= NH_2, CH_3 and Br as representative electron donating and withdrawing groups. As shown in Figure S7, electron-donating groups increase vibrational rigidity, while electron-withdrawing groups soften the vibrations, in agreement with rotational rigidity trends previously reported for UiO-66-X frameworks.[77] Despite these differences, all para-substitutions reduce $|\alpha_V|$ if compared to that of pristine UiO-66, and induce a positive thermal expansion (PTE) at increasing temperatures (see Figure S8a and Table S8). Our analysis is in agreement with previous experimental observations of lattice expansion in UiO-66-NH_2 and UiO-66-Br.[78] We attribute this suppression of NTE to two cooperating effects: the bulky Br and hydrogen-bonding NH_2 groups dampen transverse linker vibrations, while the reduction in symmetry from cubic to triclinic upon functionalization disrupts the coherent isotropic contractions responsible for the strong volumetric NTE. We performed an analogous analysis for the UiO-67 system using X= NH_2, Br, and CH_3 as substituents, revealing the same trend of reduced NTE (see Figure S8b) in agreement with previous experimental findings.[79] Interestingly, we find the transition from NTE to PTE is less likely to occur in the UiO-67 MOF derivatives if compared to the UiO-66 MOF analogues, with only the UiO-67-NH_2 system approaching positive thermal expansion near 200 K.

Having selected Br as a representative heavy substituent whose low-frequency vibrations fall within the 0–2 THz range, we further investigate how increased bromination of the BDC linker affects NTE. As shown in Figure 2e, the introduction of the 2,5-dibromo BDC in the UiO-66 MOF suppresses NTE by limiting transverse vibrations due to a higher degree of steric hindrance of the double-brominated linker if compared to that of 2-bromo BDC. Conversely, incorporating 2,6-dibromo BDC in the UiO-66 MOF activates a complementary transverse vibration mode in which half of the phenyl ring flexes, enhancing linker contractions and producing a larger NTE if compared to that of the single-brominated analogue.

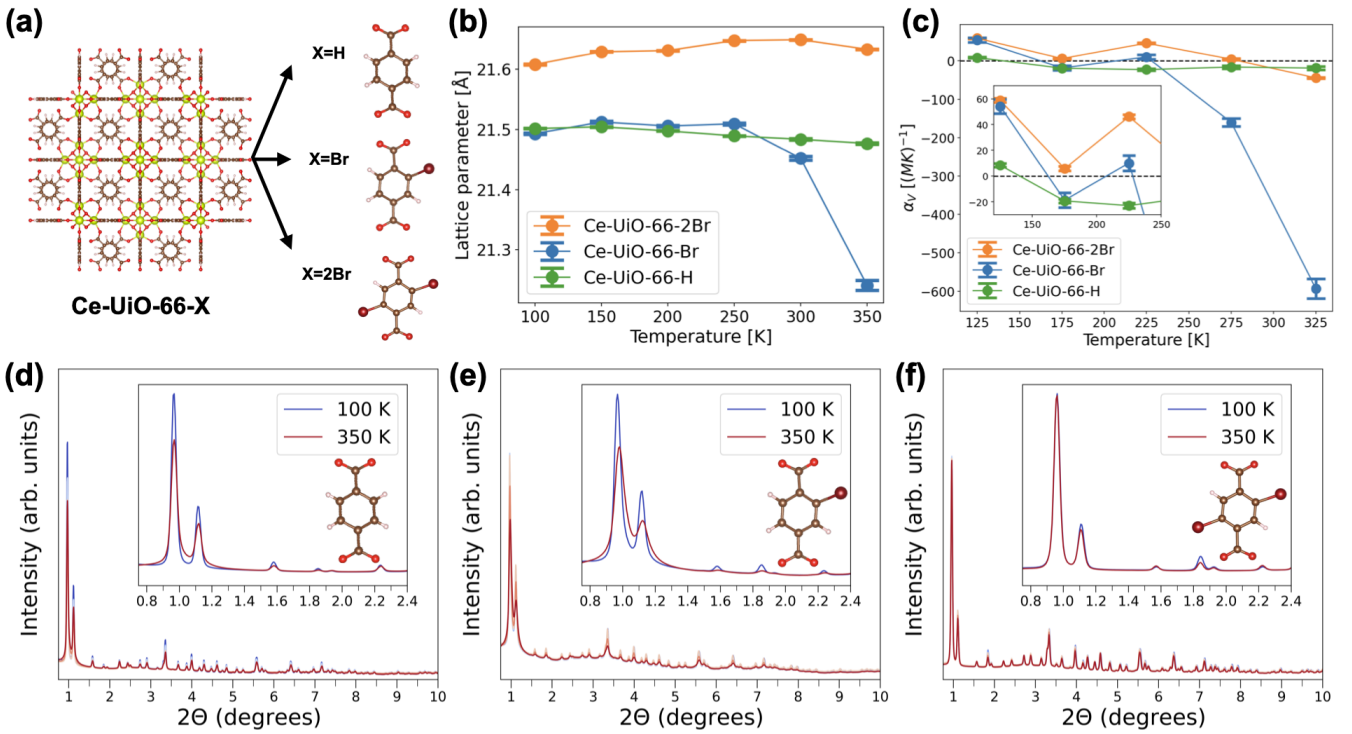

Figure 3: (a) Crystal structure of Ce-UiO-66, highlighting the molecular structures of its three BDC-derived linker variants: pristine (H), mono-brominated (Br), and di-brominated (2Br). (b) Le Bail-refined lattice parameters as a function of temperature for Ce-UiO-66-X (X = H, Br, 2Br). (c) Evolution of the volumetric thermal expansion coefficients α_V, evidencing systematic suppression of NTE with increasing bromination and an abrupt transition to colossal NTE in Ce-UiO-66-Br at elevated temperatures. (d-e) Synchrotron PXRD patterns collected between 100 and 350 K for Ce-UiO-66-H (d), Ce-UiO-66-Br (e), and Ce-UiO-66-2Br (f). A magnification of the PXRD patterns recorded at 100 and 350 K is presented in the insets of each panel.

3.2. Design Recipe

Our data-driven analysis suggests a design strategy for the engineering of NTE in MOFs: (i) select a cubic topology, with softer **pcu** leading to an increased NTE and **fcu** providing a more rigid starting framework; (ii) within a given topology, choose heavier metal nodes; (iii) favor cubic crystal systems for larger NTE; (iv) tune the length of the linker to balance the NTE and mechanical stability; (v) and functionalize the linker to further modulate the NTE while maintaining the integrity of the MOF framework.

Taken together, these design principles point toward the **fcu** topology with a BDC linker as a stable, synthetically accessible starting framework for experimental validation. This connectivity requires a tetravalent metal node, and among available options, the heavier Hf and Ce are favored by the mass–charge arguments established above. Given that NTE has been studied in thermally densified defective Hf-UiO-66[26] and pristine Zr-UiO-66,[24] we select pristine Ce-UiO-66 as a previously uncharacterized candidate predicted to exhibit enhanced NTE. To demonstrate the tunability achievable within a single MOF through linker functionalization, we also investigate the Ce-UiO-66 MOF analogues based on mono- and 2,5 di-brominated BDC variants (see Figure 3a). Computational simulations based on the established design recipe predict Ce-UiO-66 to exhibit larger NTE than Zr-UiO-66, with an increase of linker bromination leading to a progressive NTE suppression (see Figure S9).

4. Experimental Validation of Design Recipe

We experimentally validate the developed data-driven recipe for tuning NTE, focusing on the Ce-UiO-66-X= H, Br and 2Br MOFs. Figures 3b,c display the temperature-dependent evolution of the unit-cell lattice and α_V values obtained for Ce-

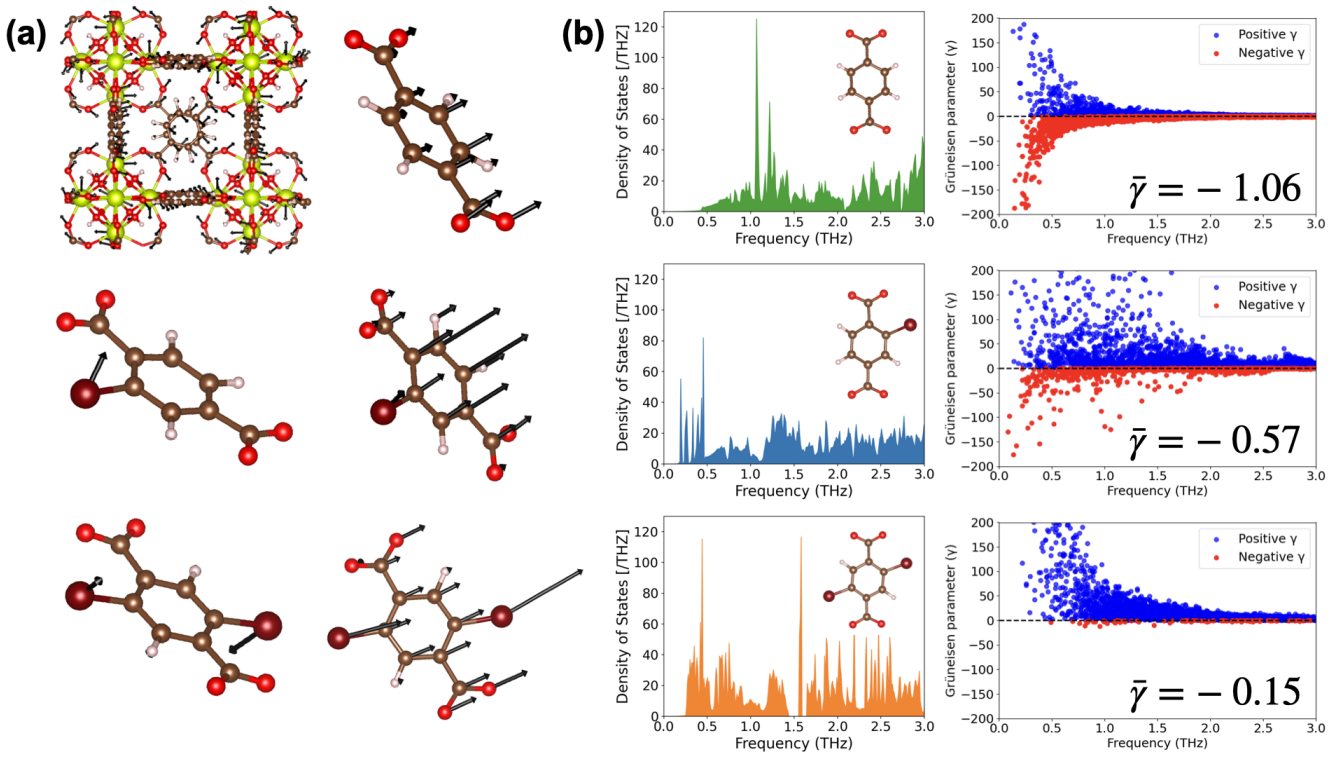

Figure 4: (a) Atomic displacements of the dominant low-frequency phonon modes in the the unit cell of pristine Ce-UiO-66 and BDC (top), 2-bromo-BDC (middle) and 2,5-dibromo-BDC (bottom) organic linkers. (b) Phonon densities of states (left panels) and Grüneisen parameter (γ) analysis (right panels) performed for the Ce-UiO-66-X= H, Br, 2Br MOFs.

UiO-66-X = H, Br, 2Br from synchrotron in situ PXRD measurements[80–83] (Figures 3d–f). In general, the experimentally determined unit-cell and α_V data agree with the trends predicted by the data-driven design recipe, with increased linker bromination progressively suppressing NTE below 250 K in the brominated MOFs compared to the pristine Ce-UiO-66-H (see Figure 3c).

Notably, pristine Ce-UiO-66-H exhibits α_V =-23(2) $(MK)^{-1}$ at 250 K, exceeding the previously reported value for Zr-UiO-66 (-16.7(8) $(MK)^{-1}$ [24]) and confirming that heavy-node substitution enhances MOF NTE. As shown in Figure 3c, mono-bromination suppresses NTE and induces PTE (+10(6) $(MK)^{-1}$ at 250K), while further NTE suppression is observed upon di-bromination, consistent with the design recipe.

To further understand the experimentally observed behavior, we performed a phonon mode analysis of the investigated Ce-UiO-66 MOFs (see Figure 4). The mode Grüneisen parameter (γ) quantifies the volumetric response per vibrational mode,[17] with more negative values indicating stronger contraction as vibrational frequency increases with temperature. All three MOFs display intense DOS features in the 0–2 THz range, but their mode-wise contributions evolve systematically with bromination. As shown in Figure 4b, an increasing number of low-frequency modes acquire positive γ as a function of Br content, offsetting the negative contributions and reducing the magnitude of the weighted average $\bar{\gamma}$. Visualization of the corresponding phonon eigenvectors in Figure 4a clarifies the microscopic origin of these trends. In pristine Ce-UiO-66-H, the lowest-frequency modes are RUMs involving rigid rotations of the metal-oxide clusters coupled to the out-of-plane transverse vibrations of the BDC linkers. These soft modes carry strongly negative γ and give rise to the large NTE observed experimentally (see Figure 4b, top panels). Mono-bromination alters the low-frequency spectrum where the lowest-frequency modes are now dominated by large-amplitude, localized Br oscillations, while the BDC linker and node clusters remain comparatively rigid (Figure 4b, middle panels). Furthermore, the transverse linker vibrations that drove NTE in the pristine Ce-UiO-66-H MOF are now increasingly impeded at higher frequency by the steric bulk of the Br substituent.

Di-bromination further increases the suppression of the NTE-driving modes where the lowest-frequency modes reflect combinatorial vibrations of the two Br groups (see Figure 4b, bottom panels), and the additional Br atom further hinders transverse linker displacements at higher frequencies leading to the lowest $\bar{\gamma}$ and weakest NTE among the series. Overall, the described atomistic harmonic phonon analysis quantitatively rationalizes the experimentally observed NTE trends and design recipe.

Beyond 250 K, Ce-UiO-66-Br undergoes an abrupt transition to colossal NTE (Figure 2c), reaching values of -161(10) and -593(25) $(MK)^{-1}$, which to the best of our knowledge are the largest MOF volumetric NTE data experimentally reported to date. This behavior above 250 K coincides with peak broadening and intensity loss in the experimental PXRD patterns (see Figure 3e), possibly due to a structural transition between 250 K and 350 K. In contrast, pristine Ce-UiO-66-H and Ce-UiO-66-2Br retain sharp diffraction features (Figures 3d and 3f, respectively) and remain highly crystalline across the full temperature range of measurement. The large-amplitude, low-frequency Br vibrations become increasingly anharmonic at elevated temperatures and likely drive this transition. While such behavior at elevated temperatures falls outside the QHA regime, the design recipe is fully consistent with the 100–250 K experimental data (refer Section S2 for further details).

5. Conclusion

In summary, we developed and experimentally validated a general strategy for tuning NTE in MOFs through targeted modification of metal node and linker chemistry while preserving framework stability. The resulting design principles identify (i) cubic topologies as favorable structural scaffolds (ii) with heavier and lower-valent metal nodes as promoters of larger NTE through softer lattice dynamics, and (iii) linker functionalization as a means to finely modulate thermal expansion. Validation on selected MOFs of the Ce-UiO-66-X (X = H, Br, 2Br) family confirms these trends and fills a gap in the experimental characterization of NTE effects in the Cerium-based UiO-66 MOFs. Beyond this validation, the eleven colossal NTE candidates identified by our screening provide promising targets for future experimental investigation. More broadly, this work shows how phonon-centric screening of databases such as PhononMOFdb can uncover the vibrational origins connecting framework structure to thermal expansion behavior, establishing design rules that guide experimental synthesis and enable the rational engineering of MOFs with targeted thermal expansion.

6. Data Availability

The database and codes will are available at https://doi.org/10.6084/m9.figshare.32050410

7. Supplementary Information

The Supplementary information is available as an additional pdf.

8. Acknowledgments

This research used computing resources of the National Energy Research Scientific Computing Center (NERSC), a Department of Energy (DOE) Office of Science User Facility and by Science and Technology Facilities Council Scientific Computing Department's SCARF cluster. P.D.K. acknowledges financial support from U.S. National Science Foundation's "The Quantum Sensing Challenges for Transformational Advances in Quantum Systems" program No. 2326838. F.T. acknowledges funding from the European Union's Horizon Europe research and innovation program under the Marie Skłodowska-Curie grant agreement No. 101201413 (AQUAFRAME). A.M.E. was also supported by the Ada Lovelace Centre at the Science and Technology Facilities Council (https://adalovelacecentre.ac.uk/), the Physical Sciences Data Infrastructure (https://psdi.ac.uk; jointly STFC and the University of Southampton) under grants EP/X032663/1 and EP/X032701/1, and EPSRC under grants EP/W026775/1 and EP/V028537/1. T.J.I acknowledges financial support from the Bakar Institute of Digital Materials for the Planet. This research was performed on APS beam time award(s) (DOI: https://doi.org/10.46936/APS-193506/60016502) from the Advanced Photon Source, a U.S. Department of Energy (DOE) Office of Science user facility operated for the DOE Office of Science by

Argonne National Laboratory under Contract No. DE-AC02-06CH11357.

References

[1] Miller, W.; Smith, C.; Mackenzie, D.; Evans, K. Negative thermal expansion: a review. *J. Mater. Sci.* **2009**, *44*, 5441–5451.

[2] Liu, Z.; Gao, Q.; Chen, J.; Deng, J.; Lin, K.; Xing, X. Negative thermal expansion in molecular materials. *Chem. Commun.* **2018**, *54*, 5164–5176.

[3] Chen, J.; Hu, L.; Deng, J.; Xing, X. Negative thermal expansion in functional materials: controllable thermal expansion by chemical modifications. *Chem. Soc. Rev.* **2015**, *44*, 3522–3567.

[4] Yang, H.; Xu, P.; Al-Maythalony, B. A.; Huang, Y.; Xu, M.; Hua, Y.; Zhang, W.; Wang, X.; Cui, S.; Zhu, H.; others Negative-thermal-expansion particles enable high-performance and ultradurable thermoelectric modules. *Sci. Adv.* **2026**, *12*, eaed3783.

[5] Zhu, Y.; Yao, G.; Liu, R.; Chen, J.; Gao, K.; Wang, M. A novel negative thermal expansion metamaterial for supersonic aerothermoelastic flutter suppression. *Aerosp. Sci. Technol.* **2025**, *165*, 110493.

[6] Dubey, D.; Mirhakimi, A. S.; Elbestawi, M. A. Negative thermal expansion metamaterials: a review of design, fabrication, and applications. *J. Manuf. Mater. Process.* **2024**, *8*, 40.

[7] Qian, J.; Long, F.; Liu, Y.; Fan, L.; Liao, M.; Gao, Q.; Lu, H.; Gao, D.; Kang, L.; Song, Y.; others Wide Temperature Zero Thermal Expansion in Al Matrix Composites with High Thermal Conductivity. *Adv. Sci.* **2026**, e75748.

[8] Makouei, S.; Nuri, H.; Nuri, M. M. R. NTE material employment in temperature resistive high sensitive fiber optic strain sensor development. *Optik* **2021**, *231*, 166395.

[9] Wu, Y.; Kobayashi, A.; Halder, G. J.; Peterson, V. K.; Chapman, K. W.; Lock, N.; Southon, P. D.; Kepert, C. J. Negative Thermal Expansion in the Metal–Organic Framework Material Cu3 (1, 3, 5-benzenetricarboxylate) 2. *Angew. Chem., Int. Ed.* **2008**, *47*, 8929–8932.

[10] Dubbeldam, D.; Walton, K. S.; Ellis, D. E.; Snurr, R. Q. Exceptional negative thermal expansion in isoreticular metal–organic frameworks. *Angew. Chem.* **2007**, *119*, 4580–4583.

[11] Zhou, W.; Wu, H.; Yildirim, T.; Simpson, J. R.; Walker, A. H. Origin of the exceptional negative thermal expansion in metal-organic framework-5 Zn 4 O (1, 4-benzenedicarboxylate) 3. *Phys. Rev. B:Condens. Matter Mater. Phys.* **2008**, *78*, 054114.

[12] Zhou, H.-C.; Long, J. R.; Yaghi, O. M. Introduction to Metal–Organic Frameworks. *Chem. Rev.* **2012**, *112*, 673–674.

[13] Furukawa, H.; Cordova, K. E.; O'Keeffe, M.; Yaghi, O. M. The Chemistry and Applications of Metal-Organic Frameworks. *Science* **2013**, *341*, 1230444.

[14] Yaghi, O. M.; O'Keeffe, M.; Ockwig, N. W.; Chae, H. K.; Eddaoudi, M.; Kim, J. Reticular synthesis and the design of new materials. *Nature* **2003**, *423*, 705–714.

[15] Wieser, S.; Kamencek, T.; Dürholt, J. P.; Schmid, R.; Bedoya-Martínez, N.; Zojer, E. Identifying the Bottleneck for Heat Transport in Metal–Organic Frameworks. *Adv. Theory Simul.* **2021**, *4*, 2000211.

[16] Hoffman, A. E. J.; Senkovska, I.; Abylgazina, L.; Bon, V.; Grzimek, V.; Dominic, A. M.; Russina, M.; Kraft, M. A.; Weidinger, I.; Zeier, W. G.; Van Speybroeck, V.; Kaskel, S. The role of phonons in switchable MOFs: a model material perspective. *J. Mater. Chem. A* **2023**, *11*, 15286–15300.

[17] Kuchta, B.; Formalik, F.; Rogacka, J.; Neimark, A. V.; Firlej, L. Phonons in deformable microporous crystalline solids. *Z. Kristallogr. - Cryst. Mater.* **2019**, *234*, 513–527.

[18] Ziman, J. M. *Electrons and Phonons: The Theory of Transport Phenomena in Solids*; Oxford University Press, 2001; Vol. 540.

[19] Takenaka, K. Negative thermal expansion materials: technological key for control of thermal expansion. *Sci. Technol. Adv. Mater.* **2012**, *13*, 013001.

[20] Evans, J. D.; Dürholt, J. P.; Kaskel, S.; Schmid, R. Assessing negative thermal expansion in mesoporous metal–organic frameworks by molecular simulation. *J. Mater. Chem. A* **2019**, *7*, 24019–24026.

[21] Elena, A. M.; Kamath, P. D.; Jaffrelot Inizan, T.; Rosen, A. S.; Zanca, F.; Persson, K. A. Machine learned potential for high-throughput phonon calculations of metal–organic frameworks. *npj Comput. Mater.* **2025**, *11*, 125.

[22] Kamencek, T.; Schrode, B.; Resel, R.; Ricco, R.; Zojer, E. Understanding the origin of the particularly small and anisotropic thermal expansion of MOF-74. *Adv. Theory Simul.* **2022**, *5*, 2200031.

[23] Ma, R.; Liu, Z.; Chen, L.; Li, Q.; Lin, K.; Chen, X.; Deng, J.; Ohara, K.; Xing, X. Transition from isotropic positive to negative thermal expansion by local Zr6O8 node distortion in MOF-801. *Microstructures* **2024**, *4*, N–A.

[24] Burtch, N. C.; Baxter, S. J.; Heinen, J.; Bird, A.; Schneemann, A.; Dubbeldam, D.; Wilkinson, A. P. Negative thermal expansion design strategies in a diverse series of metal–organic frameworks. *Adv. Funct. Mater.* **2019**, *29*, 1904669.

[25] Baxter, S. J.; Schneemann, A.; Ready, A. D.; Wijeratne, P.; Wilkinson, A. P.; Burtch, N. C. Tuning thermal expansion in metal–organic frameworks using a mixed linker solid solution approach. *J. Am. Chem. Soc.* **2019**, *141*, 12849–12854.

[26] Cliffe, M. J.; Hill, J. A.; Murray, C. A.; Coudert, F.-X.; Goodwin, A. L. Defect-dependent colossal negative thermal expansion in UiO-66 (Hf) metal–organic framework. *Phys. Chem. Chem. Phys.* **2015**, *17*, 11586–11592.

[27] Schneider, C.; Bodesheim, D.; Ehrenreich, M. G.; Crocellà, V.; Mink, J.; Fischer, R. A.; Butler, K. T.; Kieslich, G. Tuning the negative thermal expansion behavior of the metal–organic framework Cu3BTC2 by retrofitting. *J. Am. Chem. Soc.* **2019**, *141*, 10504–10509.

[28] Vornholt, S. M.; Chen, Z.; Hofmann, J.; Chapman, K. W. Node distortions in UiO-66 inform negative thermal expansion mechanisms: kinetic effects, frustration, and lattice hysteresis. *J. Am. Chem. Soc.* **2024**, *146*, 16977–16981.

[29] Yue, Y.; Mohamed, S. A.; Jiang, J. Classifying and predicting the thermal expansion properties of metal–organic frameworks: a data-driven approach. *J. Chem. Inf. Model.* **2024**, *64*, 4966–4979.

[30] Dove, M. T.; Wei, Z.; Phillips, A. E.; Keen, D. A.; Refson, K. Which phonons contribute most to negative thermal expansion in ScF3? *APL Mater.* **2023**, *11*.

[31] Rappe, A. K.; Casewit, C. J.; Colwell, K. S.; Goddard, W. A. I.; Skiff, W. M. UFF, a full periodic table force field for molecular mechanics and molecular dynamics simulations. *J. Am. Chem. Soc.* **1992**, *114*, 10024–10035.

[32] Bureekaew, S.; Amirjalayer, S.; Tafipolsky, M.; Spickermann, C.; Roy, T. K.; Schmid, R. MOF-FF – A flexible first-principles derived force field for metal-organic frameworks. *Phys. Status Solidi B* **2013**, *250*, 1128–1141.

[33] Wieser, S.; Zojer, E. Machine learned forcefields for an Ab-initio quality description of metal–organic frameworks. *npj Comput. Mater.* **2024**, *10*, 18.

[34] Bristow, J. K.; Skelton, J. M.; Svane, K. L.; Walsh, A.; Gale, J. D. A general forcefield for accurate phonon properties of metal–organic frameworks. *Phys. Chem. Chem. Phys.* **2016**, *18*, 29316–29329.

[35] Moosavi, S. M.; Novotny, B. Á.; Ongari, D.; Moubarak, E.; Asgari, M.; Kadioglu, Ö.; Charalambous, C.; Ortega-Guerrero, A.; Farmahini, A. H.; Sarkisov, L.; others A data-science approach to predict the heat capacity of nanoporous materials. *Nat. Mater.* **2022**, *21*, 1419–1425.

[36] Yue, Y.; Mohamed, S. A.; Loh, N. D.; Jiang, J. Toward a Generalizable Machine-Learned Potential for Metal–Organic Frameworks. *ACS Nano* **2025**, *19*, 933–949.

[37] Kamath, P. D.; Persson, K. A. The impact of spurious imaginary phonon modes on thermal properties of Metal-organic Frameworks. *npj Comput. Mat.* **2026**,

[38] Loew, A.; Sun, D.; Wang, H.-C.; Botti, S.; Marques, M. A. Universal machine learning interatomic potentials are ready for phonons. *npj Comput. Mater.* **2025**, *11*, 178.

[39] Kraß, H.; Huang, J.; Moosavi, S. M. MOFSim-Bench: evaluating universal machine learning interatomic potentials in metal-organic framework molecular modeling. *npj Comput. Mater.* **2025**, *12*, 4.

[40] Batatia, I. et al. A foundation model for atomistic materials chemistry. *J. Chem. Phys* **2025**, *163*, 184110.

[41] Rosen, A. S.; Iyer, S. M.; Ray, D.; Yao, Z.; Aspuru-Guzik, A.; Gagliardi, L.; Notestein, J. M.; Snurr, R. Q. Machine learning the quantum-chemical properties of metal–organic frameworks for accelerated materials discovery. *Matter* **2021**, *4*, 1578–1597.

[42] Rosen, A. S.; Fung, V.; Huck, P.; O'Donnell, C. T.; Horton, M. K.; Truhlar, D. G.; Persson, K. A.; Notestein, J. M.; Snurr, R. Q. High-throughput predictions of metal–organic framework electronic properties: theoretical challenges, graph neural networks, and data exploration. *npj Comput. Mater.* **2022**, *8*, 112.

[43] Togo, A.; Chaput, L.; Tadano, T.; Tanaka, I. Implementation strategies in phonopy and phono3py. *J. Phys. Condens. Matter* **2023**, *35*, 353001.

[44] Togo, A. First-principles Phonon Calculations with Phonopy and Phono3py. *J. Phys. Soc. Jpn.* **2023**, *92*, 012001.

[45] Dymkowski, K.; Parker, S. F.; Fernández-Alonso, F.; Mukhopadhyay, S. AbINS: The modern software for INS interpretation. *Phys. B* **2018**, *551*, 443–448.

[46] Arnold, O. et al. Mantid-Data analysis and visualization package for neutron scattering and μSR experiments. *Nucl. Instrum. Methods Phys. Res., Sect. A* **2014**, *764*, 156–166.

[47] Pinna, R. S.; Rudić, S.; Parker, S. F.; Armstrong, J.; Zanetti, M.; Škoro, G.; Waller, S. P.; Zacek, D.; Smith, C. A.; Capstick, M. J.; McPhail, D. J.; Pooley, D. E.; Howells, G. D.; Gorini, G.; Fernandez-Alonso, F. The neutron guide upgrade of the TOSCA spectrometer. *Nucl. Instrum. Methods Phys. Res., Sect. A* **2018**, *896*, 68–74.

[48] Kresse, G.; Furthmüller, J. Efficient iterative schemes for ab initio total-energy calculations using a plane-wave basis set. *Phys. Rev. B* **1996**, *54*, 11169–11186.

[49] Kresse, G.; Joubert, D. From ultrasoft pseudopotentials to the projector augmented-wave method. *Phys. Rev. B* **1999**, *59*, 1758–1775.

[50] Kresse, G.; Furthmüller, J. Efficiency of ab-initio total energy calculations for metals and semiconductors using a plane-wave basis set. *Comput. Mater. Sci.* **1996**, *6*, 15–50.

[51] Kresse, G.; Hafner, J. Ab initio molecular dynamics for liquid metals. *Phys. Rev. B* **1993**, *47*, 558–561.

[52] Perdew, J. P.; Burke, K.; Ernzerhof, M. Generalized Gradient Approximation Made Simple. *Phys. Rev. Lett.* **1996**, *77*, 3865–3868.

[53] Grimme, S.; Ehrlich, S.; Goerigk, L. Effect of the damping function in dispersion corrected density functional theory. *J. Comput. Chem.* **2011**, *32*, 1456–1465.

[54] Grimme, S.; Antony, J.; Ehrlich, S.; Krieg, H. A consistent and accurate ab initio parametrization of density functional dispersion correction (DFT-D) for the 94 elements H-Pu. *J. Chem. Phys.* **2010**, *132*, 154104.

[55] Gao, L.-L.; Feng, J.-Y.; Ren, H.-M.; Li, G. High intrinsic proton conduction in cerium(IV) metal-organic framework constructed by bromine-grafted terephthalic acid. *J. Solid State Chem.* **2024**, *333*, 124597.

[56] Toby, B. H.; Von Dreele, R. B. GSAS-II: the genesis of a modern open-source all purpose crystallography software package. *J. Appl. Crystallogr.* **2013**, *46*, 544–549.

[57] Snurr, R. Q. It's an Interesting MOF, but Is It Stable? *Matter* **2019**, *1*, 26–27.

[58] Bahadur, J.; Sharma, S. K.; Kancharlapalli, S.; Mor, J.; Armstrong, J.; Sen, D. Competitive

Host–Guest and Guest–Guest Interaction Dependent Flexibility of Crystal-Size-Engineered ZIF-8: An Inelastic Neutron Scattering Study. *J. Phys. Chem. Lett.* **2025**, *16*, 5496–5505.

[59] Casco, M. E.; Rey, F.; Jordá, J. L.; Rudić, S.; Fauth, F.; Martinez-Escandell, M.; Rodriguez-Reinoso, F.; Ramos-Fernández, E. V.; Silvestre-Albero, J. Paving the way for methane hydrate formation on metal–organic frameworks (MOFs). *Chem. Sci.* **2016**, *7*, 3658–3666.

[60] Callear, S. K.; Ramirez-Cuesta, A. J.; David, W. I.; Millange, F.; Walton, R. I. High-resolution inelastic neutron scattering and neutron powder diffraction study of the adsorption of dihydrogen by the Cu (II) metal–organic framework material HKUST-1. *Chem. Phys.* **2013**, *427*, 9–17.

[61] Chen, Y.; Lu, W.; Schroder, M.; Yang, S. Analysis and refinement of host–guest interactions in metal–organic frameworks. *Acc. Chem. Res.* **2023**, *56*, 2569–2581.

[62] Lock, N.; Christensen, M.; Wu, Y.; Peterson, V. K.; Thomsen, M. K.; Piltz, R. O.; Ramirez-Cuesta, A. J.; McIntyre, G. J.; Norén, K.; Kutteh, R.; others Scrutinizing negative thermal expansion in MOF-5 by scattering techniques and ab initio calculations. *Dalton Trans.* **2013**, *42*, 1996–2007.

[63] Zhou, W.; Yildirim, T. Lattice dynamics of metal-organic frameworks: Neutron inelastic scattering and first-principles calculations. *Phys. Rev. B:Condens. Matter Mater. Phys.* **2006**, *74*, 180301.

[64] Han, B.; Cheng, Y. Benchmarking universal machine learning interatomic potentials for rapid analysis of inelastic neutron scattering data. *Mach. Learn.: Sci. Technol.* **2025**, *6*, 030504.

[65] Bahadur, J.; Sharma, S. K.; Kancharlapalli, S.; Mor, J.; Armstrong, J.; Sen, D. Competitive Host–Guest and Guest–Guest Interaction Dependent Flexibility of Crystal-Size-Engineered ZIF-8: An Inelastic Neutron Scattering Study. *J. Phys. Chem. Lett.* **2025**, *16*, 5496–5505.

[66] Casco, M. E.; Cheng, Y.; Daemen, L. L.; Fairen-Jimenez, D.; Ramos-Fernández, E. V.; Ramírez-Cuesta, A. J.; Silvestre-Albero, J. Gate-opening effect in ZIF-8: the first experimental proof using inelastic neutron scattering. *Chem. Commun.* **2016**, *52*, 3639–3642.

[67] Casco, M. E.; Fernández-Catalá, J.; Cheng, Y.; Daemen, L.; Ramirez-Cuesta, A. J.; Cuadrado-Collados, C.; Silvestre-Albero, J.; Ramos-Fernandez, E. V. Understanding ZIF-8 Performance upon Gas Adsorption by Means of Inelastic Neutron Scattering. *ChemistrySelect* **2017**, *2*, 2750–2753.

[68] Granhed, E. J.; Lindman, A.; Eklöf-Österberg, C.; Karlsson, M.; Parker, S. F.; Wahnström, G. Band vs. polaron: vibrational motion and chemical expansion of hydride ions as signatures for the electronic character in oxyhydride barium titanate. *J. Mater. Chem. A* **2019**, *7*, 16211–16221.

[69] Franchini, C.; Sanna, A.; Marsman, M.; Kresse, G. Structural, vibrational, and quasiparticle properties of the Peierls semiconductor BaBiO 3: A hybrid functional and self-consistent GW+ vertex-corrections study. *Phys. Rev. B:Condens. Matter Mater. Phys.* **2010**, *81*, 085213.

[70] Cheng, Y.; Stone, M. B.; Ramirez-Cuesta, A. J. A database of synthetic inelastic neutron scattering spectra from molecules and crystals. *Sci. Data* **2023**, *10*, 54.

[71] Henke, S.; Schneemann, A.; Fischer, R. A. Massive anisotropic thermal expansion and thermoresponsive breathing in metal–organic frameworks modulated by linker functionalization. *Adv. Funct. Mater.* **2013**, *23*, 5990–5996.

[72] Liu, Z.; Li, Q.; Zhu, H.; Lin, K.; Deng, J.; Chen, J.; Xing, X. 3D negative thermal expansion in orthorhombic MIL-68 (In). *Chem. Commun.* **2018**, *54*, 5712–5715.

[73] Lock, N.; Wu, Y.; Christensen, M.; Cameron, L. J.; Peterson, V. K.; Bridgeman, A. J.; Kepert, C. J.; Iversen, B. B. Elucidating negative thermal expansion in MOF-5. *J. Phys. Chem. C* **2010**, *114*, 16181–16186.

[74] Queen, W. L.; Brown, C. M.; Britt, D. K.; Zajdel, P.; Hudson, M. R.; Yaghi, O. M. Site-specific CO2 adsorption and zero thermal expansion in an anisotropic pore network. *J. Phys. Chem. C* **2011**, *115*, 24915–24919.

[75] Linnera, J.; Erba, A.; Karttunen, A. J. Negative thermal expansion of Cu2O studied by quasi-harmonic approximation and cubic force-constant method. *J. Chem. Phys.* **2019**, *151*.

[76] Yuan, S.; Qin, J.-S.; Lollar, C. T.; Zhou, H.-C. Stable metal–organic frameworks with group 4 metals: current status and trends. *ACS Cent. Sci.* **2018**, *4*, 440–450.

[77] Liu, B.; Chen, X.; Huang, N.; Liu, S.; Wang, Y.; Lan, X.; Wei, F.; Wang, T. Imaging the dynamic influence of functional groups on metal-organic frameworks. *Nat. Commun.* **2023**, *14*, 4835.

[78] Taddei, M.; Tiana, D.; Casati, N.; Van Bokhoven, J. A.; Smit, B.; Ranocchiari, M. Mixed-linker UiO-66: structure–property relationships revealed by a combination of high-resolution powder X-ray diffraction and density functional theory calculations. *Phys. Chem. Chem. Phys.* **2017**, *19*, 1551–1559.

[79] Goodenough, I.; Devulapalli, V. S. D.; Xu, W.; Boyanich, M. C.; Luo, T.-Y.; De Souza, M.; Richard, M.; Rosi, N. L.; Borguet, E. Interplay between intrinsic thermal stability and expansion properties of functionalized UiO-67 metal–organic frameworks. *Chem. Mater.* **2020**, *33*, 910–920.

[80] Tavani, F.; Tofoni, A.; Pietropaoli, E.; Stoian, D. C.; van Beek, W.; Marshall, K.; Pettiti, I.; Latini, A.; D'Angelo, P. Decoding the Water Harvesting Mechanism of MIL-100(Fe) Across Short- and Long-Range Length Scales. *J. Am. Chem. Soc.* **2025**, *147*, 40507–40518.

[81] Tavani, F.; Tofoni, A.; Vandone, M.; Busato, M.; Braglia, L.; Torelli, P.; Stanzione, M. G.; Armstrong, A. R.; Morris, R. E.; Colombo, V.; D'Angelo, P. A combined soft X-ray and theoretical investigation discloses the water harvesting behaviour of Mg-MOF-74 at the crystal surface. *Chem. Sci.* **2025**, *16*, 9462–9471.

[82] Mirzaei, S.; Mirzaei, M. S.; Gao, M.-Y.; Gándara, F.; Wang, K.; Tavani, F.; Zhu, H.; Proserpio, D. M.; Yaghi, O. M. Single-Crystalline Twelve-Connected Nanographene-Based Covalent Organic Frameworks. *J. Am. Chem. Soc.* **2026**, *148*, 25241–25248.

[83] Tavani, F.; Tofoni, A.; D'Angelo, P. Exploring the Methane to Methanol Oxidation over Iron and Copper Sites in Metal–Organic Frameworks. *Catalysts* **2023**, *13*.